

# Single-channel recordings of RyR1 at microsecond resolution in CMOS-suspended membranes

Andreas J. W. Hartel<sup>a,1,2</sup>, Peijie Ong<sup>b,1</sup>, Indra Schroeder<sup>c</sup>, M. Hunter Giese<sup>d</sup>, Siddharth Shekar<sup>a</sup>, Oliver B. Clarke<sup>e</sup>, Ran Zalk<sup>d,3</sup>, Andrew R. Marks<sup>d</sup>, Wayne A. Hendrickson<sup>d,e</sup>, and Kenneth L. Shepard<sup>a,2</sup>

<sup>a</sup>Department of Electrical Engineering, Columbia University, New York, NY 10027; <sup>b</sup>Department of Applied Physics and Applied Mathematics, Columbia University, New York, NY 10027; <sup>c</sup>Plant Membrane Biophysics, Technical University of Darmstadt, 64287 Darmstadt, Germany; <sup>d</sup>Department of Physiology and Cellular Biophysics, Columbia University, New York, NY 10032; and <sup>e</sup>Department of Biochemistry and Molecular Biophysics, Columbia University, New York, NY 10032

Edited by Fred J. Sigworth, Yale University, New Haven, CT, and approved January 12, 2018 (received for review July 10, 2017)

Single-channel recordings are widely used to explore functional properties of ion channels. Typically, such recordings are performed at bandwidths of less than 10 kHz because of signal-to-noise considerations, limiting the temporal resolution available for studying fast gating dynamics to greater than 100  $\mu$ s. Here we present experimental methods that directly integrate suspended lipid bilayers with high-bandwidth, low-noise transimpedance amplifiers based on complementary metal-oxide-semiconductor (CMOS) integrated circuits (IC) technology to achieve bandwidths in excess of 500 kHz and microsecond temporal resolution. We use this CMOS-integrated bilayer system to study the type 1 ryanodine receptor (RyR1), a  $\text{Ca}^{2+}$ -activated intracellular  $\text{Ca}^{2+}$ -release channel located on the sarcoplasmic reticulum. We are able to distinguish multiple closed states not evident with lower bandwidth recordings, suggesting the presence of an additional  $\text{Ca}^{2+}$  binding site, distinct from the site responsible for activation. An extended beta distribution analysis of our high-bandwidth data can be used to infer closed state flicker events as fast as 35 ns. These events are in the range of single-file ion translocations.

patch clamp | lab-on-a-chip | protein structure-and-function | CMOS

**I**on channels are transmembrane proteins that support vital cellular functions such as energy generation (1), signaling (2), and sensing (2, 3). Ion channel recordings offer a direct way to study gating mechanisms and kinetics at a single-molecule level (3–5), and are widely used in structure-and-function analyses and pharmacological research (4–6). Despite significant progress in understanding gating action on a static (6–8) and dynamic basis (7–9), the mechanisms underlying gating dynamics resolved from ion channel recordings still remain poorly understood, in part due to limits in the temporal resolution of the measurements. On the shortest time scales, molecular dynamics (MD) simulations of ion channel gating suggest single-file translocations occur at timescales on the order of 0.1–100 ns (9–12), and subdomain movement events can occur on microsecond timescales (10–13). These events cannot be resolved in typical single-channel recordings, which are typically performed at measurement bandwidths less than 10 kHz, because of signal-to-noise ratio (SNR) limitations inherent to the electronics used for these measurements.

Despite efforts to increase the recording bandwidth of commercial voltage-clamp amplifiers through after-market modifications (13–15), the bandwidth remains limited by the capacitances at the amplifier input, which result in increasing noise power at higher frequencies and limiting achievable SNRs at shorter time scales (*SI Note 1*). To maximize bandwidth for a given channel conductance (signal level), a well-optimized system must minimize noise by employing a low-noise amplifier with minimal input capacitance and tight integration of the amplifier and lipid bilayer to reduce both membrane and wiring capacitance. Recent advances in the design of transimpedance amplifiers (TIA) and in complementary-metal-oxide-semiconductor (CMOS) integrated circuits (ICs) have enabled the analyses of single channels at

temporal resolutions as short as 1  $\mu$ s for simple self-assembling channels such as alamethicin (14–16). Further developments in amplifier design have led to 100-ns resolution in recordings of DNA translocation through solid-state nanopores, opening the possibility to further improve the performance of ion channel recordings and address the gating activity of more complex channels (17, 18).

Here, we describe a prototypic high-bandwidth measurement system capable of recording the fast closed state flickering of RyR1 channels and determine how this flickering is influenced by  $\text{Ca}^{2+}$  concentration. We have optimized our measurement instrumentation to achieve bandwidths in excess of 500 kHz for RyR1. Data analyses using hidden Markov model based analysis procedures (19, 20) were used to analyze channel gating events. In addition, we employ extended beta-distribution analysis (21, 22) of these high-bandwidth data to extrapolate the observed closed state flickering dynamics to timescales as short as 35 ns.

## Results

**Measurement Platform Capacitance and Noise.** A custom CMOS amplifier was utilized for ion channel recordings (see *Supporting Information* for schematics and circuit descriptions). The total

## Significance

We present a method for measuring the conductance of ion channels at bandwidths up to 500 kHz by fabricating lipid membranes directly on the surface of a custom amplifier chip. We apply this approach to the RyR1 receptor, enabling us to identify additional closed states for calcium-dependent inactivation at microsecond temporal resolutions. Additional data analysis using extended beta distributions allows us to detect gating events as short as 35 ns, a timescale that approaches that of single-file ion translocation. These measurement techniques hold the promise of reaching timescales for studying the kinetics of ion channels, achievable now only with computer-based molecular dynamics simulations.

Author contributions: A.J.W.H., P.O., O.B.C., A.R.M., W.A.H., and K.L.S. designed research; A.J.W.H., P.O., I.S., M.H.G., S.S., and R.Z. performed research; A.J.W.H., P.O., and S.S. contributed new reagents/analytic tools; A.J.W.H., P.O., and K.L.S. analyzed data; P.O. performed post-fabrication on CMOS-IC; I.S. performed data analysis by beta distributions; M.H.G. and R.Z. purified RyR1; S.S. developed CMOS-IC; and A.J.W.H., P.O., and K.L.S. wrote the paper.

Conflict of interest statement: A.R.M. is a consultant and member of the board and chair of the scientific advisory board of ARMGO Pharma and owns shares in the company that is targeting RyR channels for therapeutic purposes.

This article is a PNAS Direct Submission.

Published under the PNAS license.

<sup>1</sup>A.J.W.H. and P.O. contributed equally to this work.

<sup>2</sup>To whom correspondence may be addressed. Email: hartel@ee.columbia.edu or shepard@ee.columbia.edu.

<sup>3</sup>Present address: National Institute for Biotechnology in the Negev, Ben-Gurion University of the Negev, Beer-Sheva 84105, Israel.

This article contains supporting information online at [www.pnas.org/lookup/suppl/doi:10.1073/pnas.1712313115/-DCSupplemental](http://www.pnas.org/lookup/suppl/doi:10.1073/pnas.1712313115/-DCSupplemental).

supports a suspended lipid bilayer that separates the top (*cis*) from the bottom (*trans*) chamber. Both chambers are connected with silver/silver-chloride electrodes, with the *trans* chamber electrode directly fabricated on the chip surface (*Methods*).

Commercial patch-clamp amplifiers in combination with conventional membrane systems, in which membranes are typically formed across 100–300  $\mu\text{m}$  diameter holes in a polytetrafluoroethylene or Delrin film, result in  $\Sigma C > 100$  pF [ $C_{\text{AMP}}$  on the order of 10–20 pF and  $C_{\text{MEM}} \sim 100$  pF (23)]. In our case,  $\Sigma C$  is less than 4 pF (with  $C_{\text{AMP}}$  only  $< 1.5$  pF and  $C_{\text{MEM}} \sim 2.5$  pF).

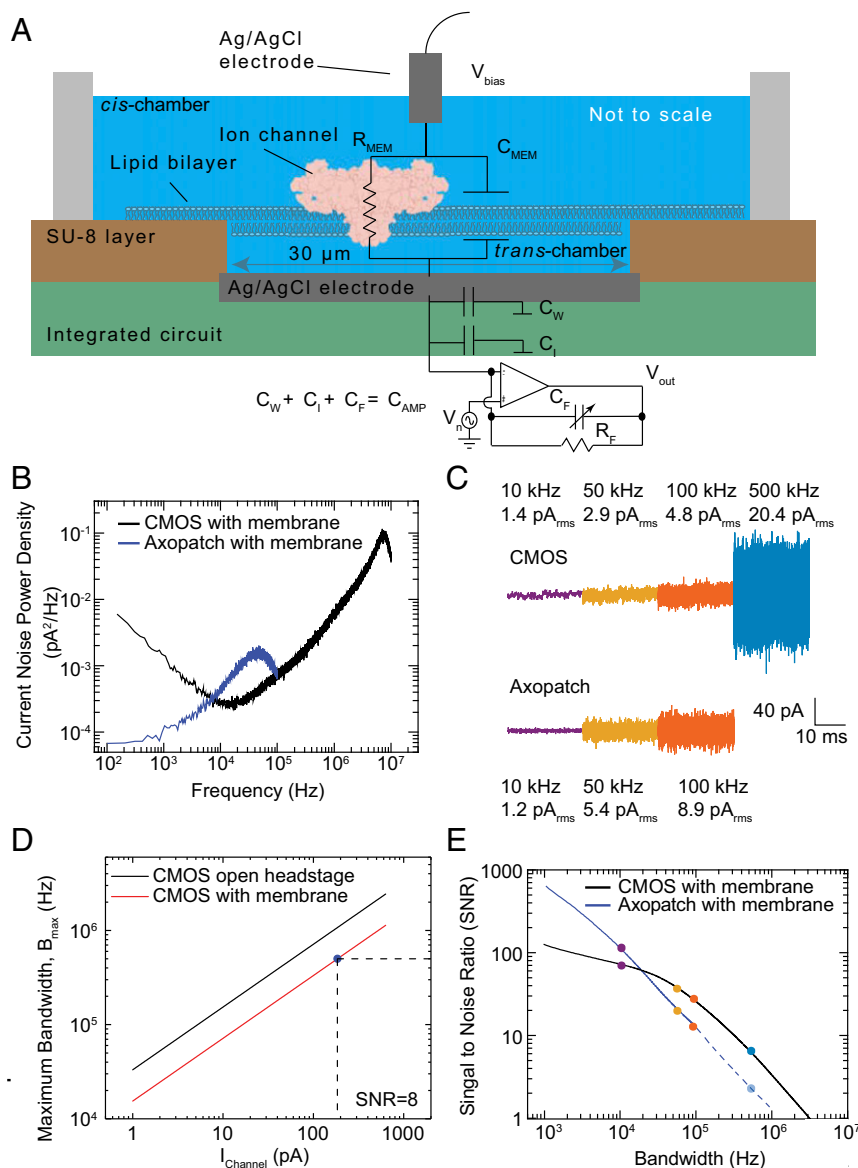


**Fig. 1.** A CMOS-integrated lipid bilayer platform. **A** shows a schematic representation of the CMOS-integrated lipid bilayer platform. A silver/silver chloride (Ag/AgCl) layer directly connects to the CMOS-integrated transimpedance amplifier (integrated circuit, green). An SU-8 microwell with a diameter of 30  $\mu\text{m}$  is photolithographically patterned over the Ag/AgCl. The lower Ag/AgCl electrode is connected through the TIA to a reference silver pellet electrode. Lipid bilayers are directly formed on top of the SU-8 layer and separate the upper *cis* chamber from the lower *trans* chamber. The circuit diagram shows the individual components of the platform and their contributions to the total capacitance. The capacitance can be divided into the membrane capacitance ( $C_{\text{MEM}}$ ) and the capacitance of the amplifier, which is the sum of the capacitance of the interconnection ( $C_{\text{W}}$ ), the input transistors ( $C_{\text{I}}$ ), and the feedback capacitor ( $C_{\text{F}}$ ).  $R_{\text{MEM}}$  represents the inverse of the channel's conductance.  $R_{\text{F}}$  represents the transimpedance gain of the amplifier. **(B)** Recorded current noise power spectral density for CMOS-integrated amplifier (black curve) and a commercial Axopatch 200B patch-clamp amplifier (blue curve) after membrane deposition. **(C)** Current noise time traces at 10 (purple), 50 (yellow), 100 (orange), or 500 (blue) kHz bandwidth. **(D)** Maximum theoretical bandwidth for different theoretical current signal levels at a set SNR of 8 for the CMOS-integrated amplifier before (black line) and after (red line) membrane deposition. **(E)** SNR-based comparison of the CMOS-integrated amplifier system (black curve) and Axopatch 200B patch-clamp amplifier (blue curve). Dotted blue curve represents extrapolated noise performance of Axopatch 200B. Circles indicate SNR corresponding to noise plotted in **C**.

Fig. 1*B* shows the noise spectrum of our system compared with a commercial measurement system using an Axopatch 200B and a lipid bilayer with a diameter of 50  $\mu\text{m}$  formed on a multielectrode cavity array (MECA) 4 chip (Ionera). The Axopatch was set to a 500-M $\Omega$  gain setting, and (as shown in Fig. 1*B*) delivers better noise performance than the CMOS-integrated amplifier below 10 kHz because of the higher flicker noise associated with the CMOS platform. However, at frequencies >10 kHz the noise performance of the CMOS-integrated amplifier begins to outperform the 200B because of the substantially lower input capacitance of the amplifier (*SI Note 1*). Fig. 1*C* shows the corresponding current noise in the time domain at different bandwidths. Fig. S2*A* and *B* show the open-headstage input-referred noise of our CMOS-integrated amplifier before the introduction of any electrolyte and after the introduction of the lipid bilayer.

The maximum measurement bandwidth ( $B_{\text{max}}$ ) is limited by the signal current,  $I_{\text{channel}}$  (Fig. 1*D*). With the noise characteristics of our amplifier, to achieve a  $B_{\text{max}}$  of  $\sim 500$  kHz at a SNR > 8 requires an  $I_{\text{channel}}$  of at least  $\sim 180$  pA. RyR1 has a single-channel conductance for potassium of up to 900 pS (24, 25). This delivers the requisite  $I_{\text{channel}}$  of 180 pA to achieve bandwidths greater than 500 kHz at 200-mV bias. The recording bandwidth of the Axopatch is limited by its antialiasing, four-pole Bessel filter, which is set to a cutoff frequency of 100 kHz. Estimating the noise performance of the Axopatch at bandwidths beyond 100 kHz to enable comparisons requires removing the effect of this filter (*SI Note 2: Axopatch Noise Extrapolation*). Fig. 1*E* shows such an SNR comparison of the two systems using the extrapolated noise performance for the Axopatch 200B. Even with the high conductance of RyR1, the SNR on the Axopatch would drop below two at a bandwidth of 500 kHz.

**Single RyR1 Measurements at High Bandwidth.** RyR1 is a homotrimeric intracellular  $\text{Ca}^{2+}$ -release channel located in the sarcoplasmic reticulum of skeletal muscle cells, and is associated with age-related  $\text{Ca}^{2+}$  leak and muscle weakness (sarcopenia) induced by oxidation of the channel (8, 17, 26, 27). Oxidation of RyR1 causes the stabilizing subunit calstabin1 (FKBP12) to dissociate from the channel complex, resulting in “leaky” channels due to increased open probability ( $P_o$ ) in low activating (*cis*)  $\text{Ca}^{2+}$  (19). As such, a detailed understanding of the  $\text{Ca}^{2+}$ -dependent gating of the RyR1 is of high interest. Recently, cryo-electron microscopy (EM) studies have revealed detailed structural models (at near-atomic resolution) for the three activating ligands  $\text{Ca}^{2+}$ , ATP, and caffeine bound at domain interfaces of the cytoplasmic core and for ryanodine in the transmembrane pore of the channel (8). RyR1 has a  $\text{Ca}^{2+}$ -dependent activation with a bell-shaped open probability dependent on the cytosolic  $\text{Ca}^{2+}$  concentration with a peak activity between 10 and 30  $\mu\text{M}$  (28). RyR1 exhibits bursts of channel activity with very fast gating events (29). These open channel bursts are interrupted by closed state events that do not reach full current levels in conventional recordings, which indicates that the recorded current signals are attenuated by limited recording bandwidth in these studies (8, 27, 30).

Purified rabbit skeletal muscle RyR1 channels in proteoliposomes were added to preformed lipid bilayers on the chip (*Methods*). Fig. 2*A–C* depicts representative single-channel recordings of RyR1 at a constant potential of  $-200$  mV. Data were filtered to bandwidths of 10, 100, 250, and 500 kHz. The current amplitude of  $\sim 180$  pA for the data filtered at 10 kHz (Fig. 2*A–C*, purple) is in good agreement with the conductivity of 870 pS determined using a conventional patch-clamp setup (Fig. S2*C*) and with previous findings (24). We also confirmed that there is no voltage dependency of the open probability at the activating  $\text{Ca}^{2+}$  concentrations of 40  $\mu\text{M}$  (Fig. S2*D*). In Fig. 2*A–C* it is also apparent that both the open channel and the closed channel noise increase with increasing bandwidth with  $I_{\text{rms}}$  of

$\sim 1.4$  pA $_{\text{RMS}}$  at 10 kHz, 4.8 pA $_{\text{RMS}}$  at 100 kHz, 10.3 pA $_{\text{RMS}}$  at 250 kHz, and 20.4 pA $_{\text{RMS}}$  at 500 kHz. At 500 kHz, an SNR of  $\sim 8$  can be achieved, allowing full openings as short as 2  $\mu\text{s}$  to be resolved, which is, to our knowledge, the fastest single recording of a ligand-gated ion channel.

At 500 kHz, there are a large number of gating events in the low microsecond timescale. These events are either partially (Fig. 2*D* and *E*) or completely unresolved (Fig. 2*F*) at lower filter bandwidths. Lack of resolution of these gating events continues to be present even at 500 kHz, indicating that recording their dynamics could be beyond our measurement capabilities. Fig. 2*G–I* shows examples of gating events as short as 2–3  $\mu\text{s}$ , approaching the  $\sim 2$   $\mu\text{s}$  temporal resolution limit of our instrument (vertical bars indicate events). The very fast open channel events in Fig. 2*G* and *I* are poorly resolved at 100- or 250-kHz bandwidths, and only approach the full current amplitude of  $\sim 180$  pA at 500 kHz. In addition, the open channel events in Fig. 2*G–I* (marked with asterisks) show examples of channel-gating events between subconducting states of RyR1 that are sometimes present in these traces. In Fig. 2*G* and *I*, the channel undergoes a transition from the closed state to an open state at  $\sim 80\%$  conductance for a duration of  $\sim 5$   $\mu\text{s}$  and then shows a bandwidth-limited gating event to the full conducting state. In Fig. 2*H* the channel shows a transition from the closed state to the full open state with a brief dwell ( $\sim 3$   $\mu\text{s}$ ) at a subconducting state at half-amplitude. All of our subsequent analysis of conduction dynamics will treat any subconductance states as full open channel events.

To provide a more comprehensive analysis of the impact of recording bandwidth on amplitudes and dwell times, a representative 1-s-long conductance trace is idealized using the segmental K-means (SKM) method in QuB. These idealized data are used to identify open state events and dwell times, and  $I_{\text{channel}}$  is then determined as the average open channel current during this event duration. This analysis averages the effects of subconductance states, which may actually be present within the open channel dwell time event. Fig. 3*A* shows the current amplitudes and open dwell times at different bandwidths, indicating the effect of bandwidth on the amplitude of fast gating events. The data filtered to 10 kHz show the longest open channel dwell times and lowest current amplitudes. With increasing bandwidth, the dwell times become shorter and the current amplitudes increase (Fig. 3*B*). Fig. 3*B*, Inset, shows the current amplitude histograms for brief events with durations below 10  $\mu\text{s}$  at 250- and 500-kHz bandwidths. The histogram shows that the short events at full amplitude are relatively rare but are still resolvable because they are within the temporal resolution at these bandwidths. Because the events are less attenuated at 500 kHz, there is a shift in the histogram toward the full 180-pA amplitude. The dwell time histogram of the open channel events (Fig. 3*C*) at different bandwidths shows a much larger number of events at 500 kHz. The overall number of open channel events of a duration of up to 100  $\mu\text{s}$  increases by  $\sim 150\%$  from 4,694 to 6,988 events per second when the bandwidth is increased from 50 to 500 kHz. However, the open probabilities remain largely unaltered.

**$\text{Ca}^{2+}$ -Dependent Modulation of RyR1 Gating.** Ryanodine receptors exhibit a bell shaped  $\text{Ca}^{2+}$ -dependent gating behavior (28). For RyR1, the channel is closed ( $P_o \sim 0$ ) at low nanomolar  $\text{Ca}^{2+}$  concentrations (in the *cis* chamber), and is activated at micromolar concentrations ( $P_o \sim 1$ , in the presence of activating micromolar  $\text{Ca}^{2+}$  and millimolar ATP and/or caffeine). The channel is inactivated at  $\text{Ca}^{2+}$  concentrations in the low millimolar range. The activating  $\text{Ca}^{2+}$  binding site is located, along with the activating binding sites for ATP and caffeine, within the carboxyl-terminal domain (CTD) of the channel (8). Once activated, RyR1 shows bursts of very high open probability interrupted



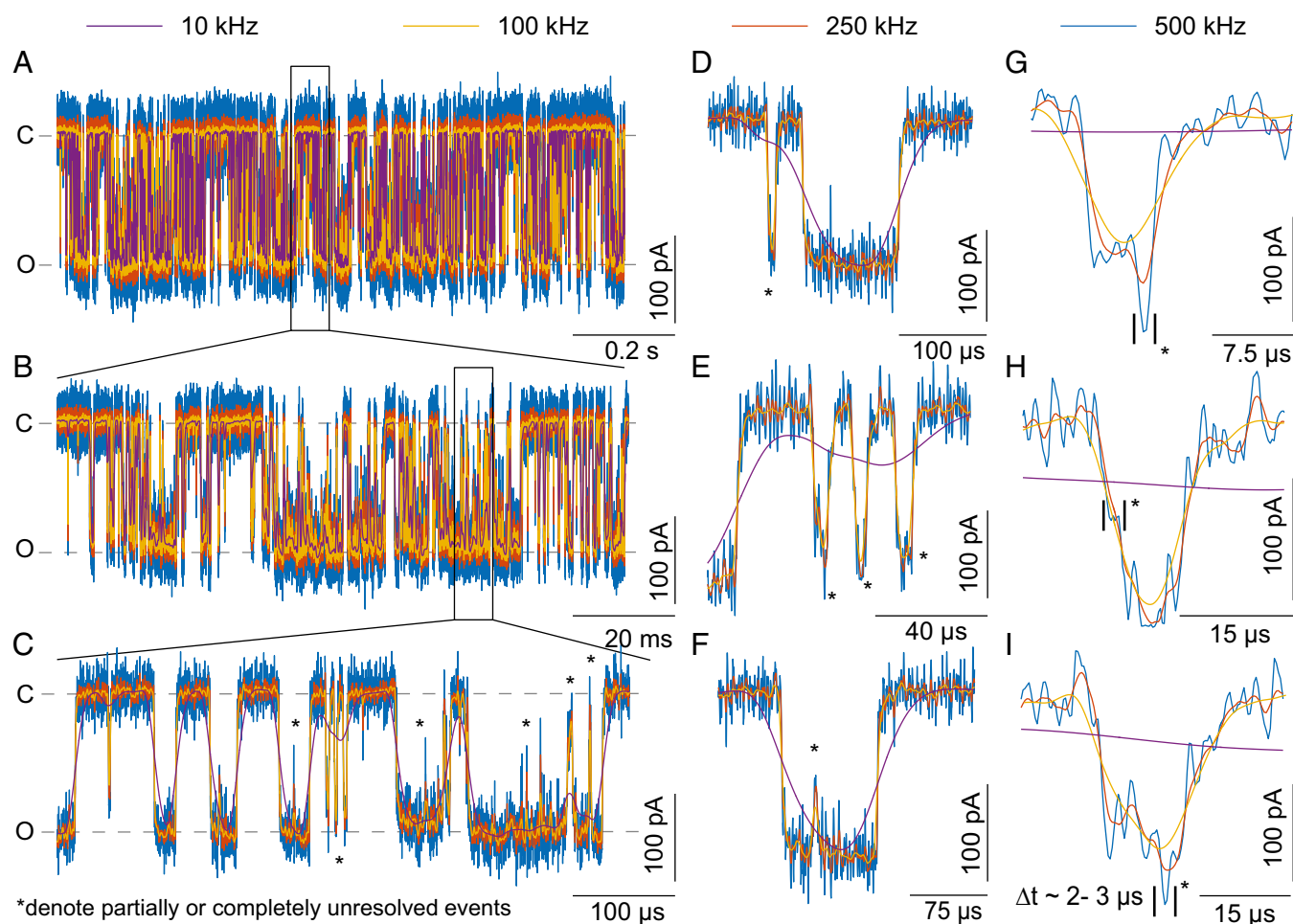


**Fig. 2.** Increase in bandwidth results in the resolution of fast gating events. Data were recorded at a sampling rate of 40 million samples per second and digitally filtered using a four-pole Bessel filter. A through I show single RyR1 single-channel recordings at different digital filter cutoff frequencies of 10 (purple), 100 (yellow), 250 (orange), and 500 (blue) kHz. A–C show a stepwise magnification into a representative segment of channel bursts. The asterisks denote exemplary gating events that are either partially (D and E) or completely unresolved (F–I) at the limited bandwidth. Vertical bars indicate duration of events.

by closing events with very short dwell times. The detailed dynamics of these closed state flicker events are usually obscured in conventional recordings due to bandwidth limitations.

In this present study, the recordings from our CMOS-integrated amplifier were analyzed using the single-molecule analysis software package QuB (20) with segmental K-means- (SKM-) based idealization and maximum likelihood estimation of rate constants (*Methods*). Data were filtered to 10, 100, 250, and 500 kHz, and the gating kinetics were modeled with two open states ( $O_1$  and  $O_2$ ) and two closed states ( $C_S$  and  $C_F$ ), a model consistent with the most recent structural considerations (8). The open channel states are both assigned the full open current amplitude, resulting in an equivalent treatment of all subconducting states as open channel events. This model, shown in Fig. 4A, has connections between the two open states and between the two closed states, as well as two linking connections between open and closed states. The model selection process is outlined in *SI Note 3: Model Selection*. Because this model is used for all of the  $\text{Ca}^{2+}$  concentrations considered, the states may represent different physical structures. Fig. 4B–D shows the single-channel current traces at three different  $\text{Ca}^{2+}$  concentrations (<20 nM, 40  $\mu\text{M}$ , and 400  $\mu\text{M}$ ) at a conventional bandwidth of 10 kHz, allowing one to visualize the influence of  $\text{Ca}^{2+}$  on the open probability ( $P_o$ ) of RyR1. At a concentration of <20 nM free

$\text{Ca}^{2+}$  (below the detection limit of a Fura-2 assay of free  $\text{Ca}^{2+}$ ) and in the presence of 5 mM ATP, the RyR1 recordings only show very sparse current spikes resulting in a  $P_o < 0.01$ . At a  $\text{Ca}^{2+}$  concentration of 40  $\mu\text{M}$  (with 5 mM ATP added), RyR1 is almost exclusively in the open state ( $P_o > 0.90$ ) and shows an abundance of fast flicker events. When the  $\text{Ca}^{2+}$  concentration is increased to 400  $\mu\text{M}$ , the open probability decreases to  $P_o \sim 0.50$ .

Fig. 4F–H displays a more detailed view of the dwell time distributions for the closed and open channel events at bandwidths of 10 and 500 kHz, i.e., at a temporal resolution of 100 and 2 ms, respectively (see also Figs. S4, S5, and S6). As expected, due to an increase by almost a factor of 2 in the detection of unresolved events, the relative dwell time distributions of the 500-kHz measurements are shifted toward shorter durations. A closer inspection of these dwell times shows that the time constant for one of the two closed states ( $C_S$ ) in the model is temporally determined at a bandwidth of less than 10 kHz. However, the time constant for the second closed state ( $C_F$ ) is strongly influenced and limited by the measurement bandwidth. Fig. 4E tabulates the time constants of the open and closed states as determined by maximum interval likelihood (MIL) estimation using QuB at 10- and 500-kHz filter bandwidths and three different  $\text{Ca}^{2+}$  concentrations, <20 nM, 40  $\mu\text{M}$ , and 400  $\mu\text{M}$  (see also Fig. S7A–C and Table S1).

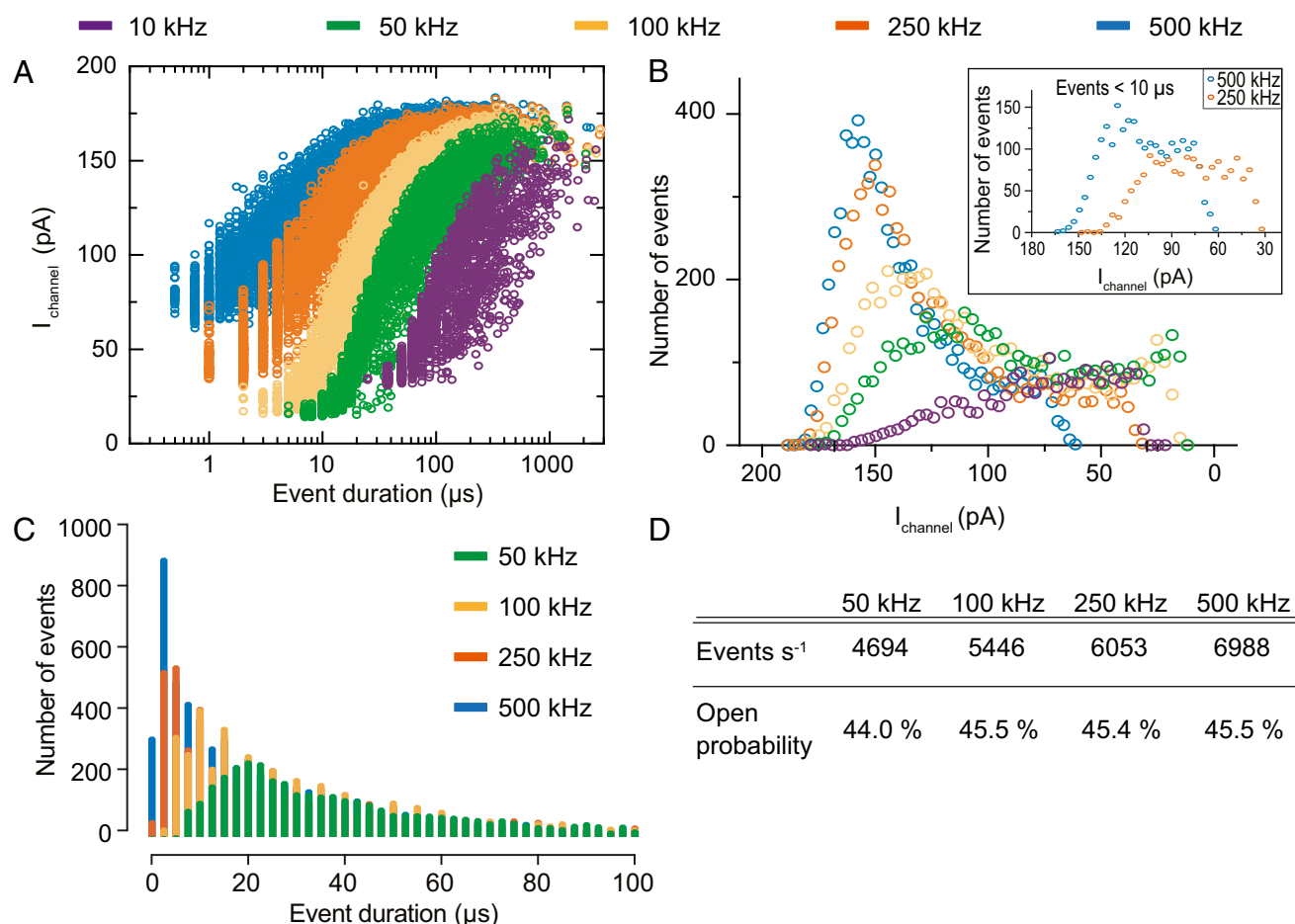


**Fig. 3.** Open channel analyses of RyR1 recordings at high bandwidth. Recordings were performed in the presence of 400- $\mu$ M free  $\text{Ca}^{2+}$ , 1 M KCl, 20 mM Hepes, pH 7.4, 5 mM ATP at a constant voltage across the membrane of  $-200$  mV. Data were recorded at a sampling rate of 40 million samples per second and digitally filtered using a four-pole Bessel filter with a cutoff frequency of 10 (purple), 50 (green), 100 (yellow), 250 (orange), and 500 (blue) kHz. Data are decimated to an effective sample rate of 8 times the cutoff frequency, and results are shown for analysis of a representative 1-s-long trace. Single channel openings were detected using the SKM method in the QuB software package. *A* shows a plot of the current amplitudes and the respective dwell times of the channel opening events. *B* depicts the relative distribution of current amplitudes detected with different filter cutoff frequencies. *Inset* shows amplitude histograms of events  $< 10$   $\mu$ s at 250 (orange) and 500 (blue) kHz filter cutoff frequency. *C* shows a dwell time histogram of channel opening events and the influence of the increase of the cutoff frequency. *(D)* Number of events per second and open probability at different cutoff frequencies.

For the 400- $\mu$ M  $\text{Ca}^{2+}$  concentration (Fig. 4*H*) at 500 kHz, the existence of  $C_F$  is immediately evident with a time constant in the microsecond range. Occupancy in  $C_S$  and  $C_F$  are represented in the dwell time histogram at 10 kHz (purple bars in Fig. 4*H*) by a single distribution, making  $C_S$  and  $C_F$  indistinguishable at this bandwidth. This single peak in the dwell time distribution at 10 kHz separates into two distinct distributions representing  $C_S$  and  $C_F$  when analyzed at 500 kHz. The  $\text{Ca}^{2+}$ -dependent inactivation of RyR1 is apparent when comparing the prominent and distinct  $C_S$  distribution at 400  $\mu$ M with the more obscure and overlapping distribution in the 40- $\mu$ M histogram. The time constants for the open state under both 40- and 400- $\mu$ M  $\text{Ca}^{2+}$  concentrations appear relatively unchanged, which corresponds to the full binding of  $\text{Ca}^{2+}$  to the activating binding site. Additionally, the greater dwell time separation between  $C_S$  and  $C_F$  with increasing  $\text{Ca}^{2+}$  concentration from 40 to 400  $\mu$ M corresponds to the binding of  $\text{Ca}^{2+}$  to the inactivating site. This finding is consistent with previous structural studies of RyR1 (31).

A similar effect is observed in Fig. 4*F* for  $C_S$  and  $C_F$  at the lowest  $\text{Ca}^{2+}$  concentration ( $< 20$  nM), which are only distinguishable at 500 kHz. Based on the comparably slow dwell times in the closed states and the fast dwell times in the open states, we

attribute the transitions in this case to the more rigid closed state structure of the RyR1 channel found at  $\text{Ca}^{2+}$ -free and pre-activating conditions (8). Here, the dwell time distribution of the open states is shifted toward shorter event durations at 500-kHz bandwidth due to the nature of the fast open channel flicker events, which are poorly resolved at low bandwidth. Some further insight into the channel gating can be inferred from the 500-kHz data at different  $\text{Ca}^{2+}$  concentrations. The rate constants (Fig. S7 *D–F*) for the open-to-open transitions all remain relatively slow ( $< 1,000$  s<sup>-1</sup>), independent of  $\text{Ca}^{2+}$  concentrations. The transitions between the open and closed states, however, have both fast and slow rate constants. The disparity between the rates within a given  $\text{Ca}^{2+}$  concentration suggests preferential structural pathways between the open and closed states.

**Nanosecond Gating of RyR1.** Even at 500 kHz, we hypothesize that there exist faster transitions to the closed state that are still outside the range of available bandwidth in the measurement. To extrapolate to these shorter time scales, we performed the extended beta distribution analysis. In this approach, it is recognized that closing events that are attenuated by limited bandwidth appear as excess open channel noise (22). With the appropriate modeling assumptions, the gating dynamics can be



inferred (Methods; SI Note 4: Extended Beta-Distribution Analysis). For the beta distribution, we use the model shown in Fig. 5A. In this model, we focus on the transitions between one combined open state and three closed states with different kinetics. The closed states are represented as a slow closed state ( $\beta_S$ ), a medium-fast closed state ( $\beta_M$ ), and a very fast closed state ( $\beta_F$ ). Since the beta-distribution analysis does not consider the sequence of events and only analyzes transitions between the open state and the closed states, transitions between the closed states are not represented in this model.

Fig. 5B shows the amplitude histogram resulting from beta-distribution analyses of the 40- $\mu$ M  $\text{Ca}^{2+}$  recordings. Under these conditions, the channel remains in the burst state at all times. The broadening and asymmetry of the open channel distribution is due to transitions to the very fast closed state ( $k_{OF}^\beta$ ), and the extended tail slope region toward lower current amplitudes is due to transitions into the medium-fast closed state ( $k_{OM}^\beta$ ). Finally, the plateau region approaching the closed state current corresponds to transitions to the slow closed state ( $k_{OS}^\beta$ ). Fig. 5C and D shows the rate constants of the RyR1 gating determined using the beta fit at different bandwidths (10, 100, 250, and 500 kHz). We find that at a given filter frequency, the rate constants for transitions to the slow closed state  $\beta_S$  determined with the beta distribution are in good agreement with the transitions to  $C_F$  noted using the QuB-based analysis (Table S2), implying equivalence of these states in our analyses.

The results of Fig. 5C and D also demonstrate one of the limitations of the beta-distribution analysis. As expected, we find that at low bandwidths (10 kHz), the rate constants for  $\beta_M$  and  $\beta_F$  are no longer distinguishable because of insufficient bandwidth in the measurement. However, we also find this to be true at 500 kHz, because of the reduced SNR at this bandwidth. The beta-distribution technique extracts information from the “excess” noise, making noise and signal indistinguishable when the SNR is significantly less than  $\sim 10$ . Furthermore, at high bandwidth, the root-mean-square contributions from Johnson and shot noise should be taken into account (SI Note 4: Extended Beta-Distribution Analysis). Despite these limitations, using data at a 250-kHz bandwidth with an SNR of more than 15, we are able to infer two very short closed states,  $\beta_M$  with a dwell time of  $\sim 300$  ns and  $\beta_F$  with  $\sim 35$  ns.

## Discussion

By developing new instrumentation for high bandwidth CMOS-integrated conductance measurements, we have been able to measure fast ion channel gating kinetics of  $\text{Ca}^{2+}$ -dependent activation and inactivation in the RyR1 channel. Our data show that the  $\text{Ca}^{2+}$ -dependent activation (at 40  $\mu$ M) of RyR1 is linked with closed state flickering as seen in dwell-time-based analysis using QuB. Further analyses with extended beta distributions reveal that the fast state ( $C_F$ ) detected at 40- $\mu$ M  $\text{Ca}^{2+}$  with QuB can be further resolved into a very fast state ( $\beta_F$ ) and a medium-fast state ( $\beta_M$ ). The medium-fast events show time constants of  $\sim 300$  ns, and the very fast events show time constants as short as 35 ns. In addition, we are able to demonstrate that the  $\text{Ca}^{2+}$ -dependent inactivation is associated with an additional closed state with a dwell time in the order of  $\sim 100$   $\mu$ s. The coexistence of two independent  $\text{Ca}^{2+}$ -dependent closed states strongly supports the presence of an additional  $\text{Ca}^{2+}$  binding site, distinct from the site responsible for activation (31).

Cryo-EM studies have investigated the structure of RyR1 in both the open and closed states (8, 26, 27). These studies have suggested that  $\text{Ca}^{2+}$  activation results from  $\text{Ca}^{2+}$  binding in the C-terminal domain (CTD), which leads to conformational changes and increases the likelihood of the channel pore opening. A cascade of domain movements ultimately causes the S6 transmembrane helices to move outward, increasing the pore diameter and allowing permeation of  $\text{Ca}^{2+}$  cations. Collective

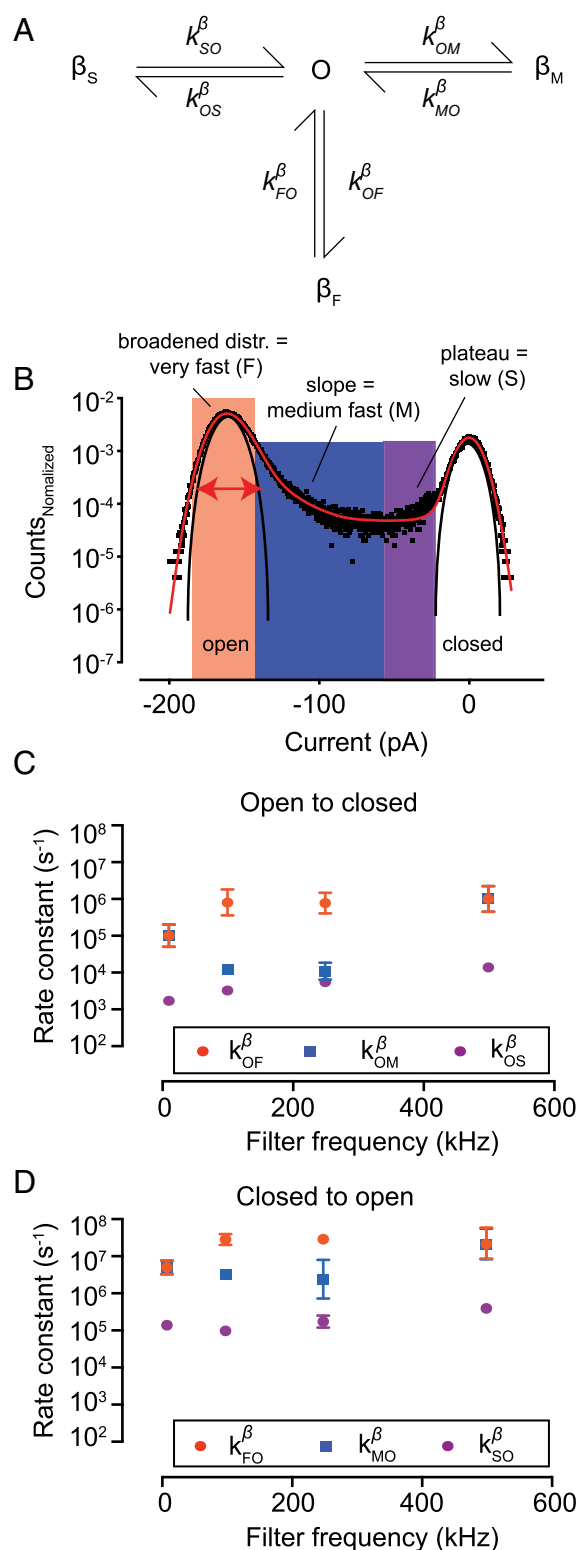


**Fig. 5.** Analyses of high bandwidth single-channel recordings using beta distribution. (A) Markov model used for beta distribution analyses including a slow closed state ( $\beta_S$ ), an intermediate closed state ( $\beta_M$ ), a fast closed state ( $\beta_F$ ), one open state, and the respective rate constants per state transition. (B) Amplitude histogram of single-channel recordings and fit by beta distribution. The closed and open state noise are indicated by the two Gaussian shaped functions. Broadening of the Gaussian shaped distribution in the open state noise is attributed to very fast ion channel gating events. Rate constants for the closed (C) and open state (D) of the fast (orange circles), intermediate (blue squares), and slow (purple circles) states. Plotted rate constants are geometric means  $\pm$  geometric SD.



thermal motions on the timescale of milliseconds were attributed to the stochastic openings of the channel, consistent with the kinetics obtained from previous single-channel recordings limited to 0.5–10 kHz bandwidth (32); however, this explanation is insufficient for the dynamics observed in this study. These structural studies offer new insights into RyR1 gating, but they only provide the starting and ending state, leaving the dynamics of the transition to be determined.

Our results suggest that subdomain movements may be involved in microsecond (represented by  $C_F$ ) and nanosecond events (represented as  $\beta_F$  in Fig. 5A), instead of large-scale movements associated with long dwell time gating events. NMR experiments of enzymes have determined that the timescale of movements in subdomains (nanosecond to microsecond timescales) is orders of magnitude faster than in larger domains (microseconds to seconds timescales) (13). We hypothesize that the fastest events could be attributed to stochastic motions of the S6 helices themselves. With the surrounding domains in their proper position for the open channel structure, inward movements of the S6 helices shrink the channel blocking the single-file passage of hydrated ions, which we observe as fast closed state flickering. For slower gating events in the microsecond timescale, the S4–S5 linker, which directly couples with the S6 helices may be moving in tandem from thermal motion, causing enough of a perturbation in the pore to cause it to open or close. The fast gating events reported here are significantly faster than the on rates reported for  $\text{Ca}^{2+}$  binding. Typically, fast  $\text{Ca}^{2+}$  binding on rates are limited by  $\text{Ca}^{2+}$  diffusion and found to be in the range of  $10^8$ – $10^9 \text{ M}^{-1} \text{ s}^{-1}$  (33–35), which translates into a time constant for binding of 2.5 and 100  $\mu\text{s}$  for the range of concentrations used in this study (30 nM to 400  $\mu\text{M}$ ). This supports the notion that bulk structural changes resulting from  $\text{Ca}^{2+}$  binding lead to an open state conformation and smaller movements near the pore result in much faster gating.

The mean passage time for a single ion through an ion channel is dependent on its conductance and the applied voltage but typically in the order of 0.1–100 ns, which sets an upper limit for bandwidth requirements (10–12). One goal of electrophysiology is to gain a better understanding of the structure/dynamics relations of ion channels. This can be achieved, for example, by combining experimental data with in silico MD simulations. Typically MD simulations are performed, depending on the size of the simulated protein, over a time window between a few nanoseconds up to several microseconds (or, in some cases, milliseconds) (9, 36). MD simulations of large and complex protein structures such as RyR1 remain very challenging and require computing resources far beyond the scope of this study. The present data show, however, that we are able to extend the temporal resolution into the timescales of a mean passage time.

In this study, we use the RyR1 channel because of its high conductance (e.g., up to 900 pS for  $\text{K}^+$ ). This allows us to perform measurements at bandwidths up to 500 kHz. Due to the complex gating behavior of the RyR1 channel, we chose to perform our studies at a relatively high SNR of eight. A channel with less complex gating behavior could potentially tolerate an SNR as low as four. This in turn, would allow the measurement techniques here to be applied to ion channels with conductance of  $\sim 450$  pS. Although still a high conductance, there are a number of ion channels that could be studied, including the BK channel and bacterial homologs, such as MthK, or the large-conductance mechanosensitive channels (MscL) (37, 38). Further reduction of the membrane size and improvements in the electronics have the potential to extend these techniques to lower conductance channels.

We conclude that the combination of state-of-the-art electronics and leading-edge analysis tools has the potential to bridge the gap between theoretical simulations and experimental observations.

## Methods

**IC Design and Supporting Circuitry.** The IC was designed and fabricated in a conventional 0.18- $\mu\text{m}$  CMOS process. The  $5 \times 5$  mm chip consists of 25 TIAs, each of which occupy an area of  $400 \times 400 \mu\text{m}$  and support a maximum recording bandwidth of 10 MHz. The peripheral circuitry required for proper functioning of the chip were assembled on a custom-designed printed circuit board (PCB). The TIA gain is programmable through components on the PCB but was set to 50 M $\Omega$  for the experiments in this work. The analog output voltage is filtered in hardware using a four-pole Bessel filter with a cutoff frequency of 10 MHz before being sampled at 40 million samples per second. The sampled data are then fed into a field-programmable gate array (FPGA) (Opal Kelly XEM6310). Custom Python code running on a host PC then acquires this data from the FPGA over a USB 3.0 link.

**CMOS Die Postprocessing.** The CMOS die was first bonded with polydimethylsiloxane (PDMS; Sylgard 184; Dow Corning) to a glass slide, which served as a handle substrate during all of the chip postprocessing. A layer of Shipley 1813 photoresist (Microchem) was spun onto the chip at 3,000 rpm for 60 s and baked at 115  $^{\circ}\text{C}$  for 1 min. The photoresist was exposed on a Süss MicroTec MA6 mask aligner with a dose of 96 mJ/cm $^2$  to open  $150 \times 150 \mu\text{m}$  windows around the aluminum electrodes. This opening was used to first etch the aluminum in a heated bath of aluminum etchant (Transene type A) for 60 s at 60  $^{\circ}\text{C}$ . The photoresist also served as a liftoff mask for the metallization. The metal stacks, which composed of 5 nm of Ti and 400–500 nm Ag, were electron beam evaporated (Angstrom EvoVac). The photoresist was stripped in an acetone bath overnight.

The chip surface was then primed with hexamethyldisilazane (HMDS-100%) (Transene), which was applied to the surface of the chip and spun dried at 3,000 rpm for 60 s. Next, SU-8 3005 (Microchem) was spun onto the chip at 2,000 rpm for 60 s with an initial 10-s spreading stage at 500 rpm for 10 s, giving a 7- $\mu\text{m}$ -thick layer. The SU-8 was soft baked at 65  $^{\circ}\text{C}$  for 2 min. Next, 30- $\mu\text{m}$  circular openings in the SU-8 were patterned on an EVG 620 mask aligner with a dose of 300 mJ/cm $^2$ . A postexposure bake was done at 65  $^{\circ}\text{C}$  for 1 min. Finally, the chips were soaked in SU-8 developer (Microchem) for 20 s and rinsed with isopropyl alcohol. The die was released from the PDMS by soaking in hexane for 2 h.

**Chip Packaging and Microelectrode Chlorination.** The amplifier dies were wire bonded to a 272-pin ball-grid array (BGA) package and doughnut encapsulated with epoxy. LED 401 (Masterbond) was used as a dam epoxy and OG 116–31 (EPO-TEK) was used as the fill epoxy to protect the wire bonds.

A 1-cm section of cylindrical polypropylene tubing served as a fluid reservoir. The chamber was attached to the epoxy with KWIK-CAST silicone (World Precision Instruments) to form a water-tight seal. Additionally, silicone was used to cover all nonactive electrodes. The surface of the silver microelectrode was chlorided by applying a 1-mL drop of concentrated bleach onto the surface for 60 s. Between experiments the fluid chamber and chip and external Ag/AgCl pellet electrode were rinsed thoroughly with ethanol and deionized water. Bleach was reapplied to the silver whenever the chloride layer visually appeared to be depleted.

**Purification of RyR1.** RyR1 complex was purified from rabbit (*Oryctolagus cuniculus*) skeletal muscle as previously described (32). Flash-frozen rabbit skeletal muscle (100 g) was blended for 90 s in 500 mL of ice-cold homogenization buffer containing 10 mM Tris-maleate, pH 6.8, 1 mM DTT (DTT), 1 mM EDTA, and 150  $\mu\text{M}$  phenylmethylsulfonyl fluoride (PMSF). The supernatant following centrifugation of the mixture for 10 min at  $8,000 \times g$  was collected and centrifuged for 20 min at  $40,000 \times g$ . Pellets were detergent solubilized in 50 mL buffer containing 1% CHAPS, 1 M NaCl, 10 mM Hepes, pH 7.4, 1 mM EDTA, 0.1% phosphatidylcholine, 1 mM DTT, 1 mM benzamide, 150  $\mu\text{M}$  PMSF, and a protease inhibitor mixture tablet (Roche). Following 20 up/down strokes in a glass-glass homogenizer, the mixture was diluted with a buffer identical to the solubilization buffer but without NaCl and the protease inhibitor mixture tablet. The diluted mixture was centrifuged for 30 min at  $100,000 \times g$ , the supernatant collected and filtered through a 0.2- $\mu\text{m}$  filter and looped overnight at 4  $^{\circ}\text{C}$  through a 5 mL GSTrap (GE healthcare) column with FKBP12 (calstabin1) bound. The column was washed with 50 mL of modified solubilization buffer (0.5% CHAPS and 0.5 M NaCl) and elution buffer, identical to the buffer used for the wash but with the addition of 10  $\mu\text{M}$  FKBP12.6 (calstabin2) that was expressed in 1 L IPTG-induced transformed BL-21 cells, loaded onto a GST column and collected following thrombin cleavage for 1 h at room temperature. Calstabin2 was used for elution because it has a higher affinity for RyR1 than the physiological subunit (calstabin1, FKBP12). The eluent containing RyR1 and



calstabin2 was collected (~10 mL) and concentrated on a 100 kDa cutoff centrifugation filter (Millipore) to 1 mL.

**Reconstitution of RyR1 into Microsomes.** Purified RyR1 with calstabin2 (FKBP12.6) was reconstituted into microsomes as described by Lee et al. (39). In brief, sample containing purified receptor complex was added to 5 mg/mL of lipid mixture [5:3 molar ratio of 1,2-dioleoyl-*sn*-glycero-3-phosphoethanolamine (DOPE)/1,2-dioleoyl-*sn*-glycero-3-phosphocholine (DOPC)] and placed in a dialysis bag. The sample containing Chaps was dialyzed overnight in 1 L of buffer containing 0.5 M NaCl, 0.1 mM EGTA, 0.2 mM CaCl<sub>2</sub>, 150  $\mu$ M PMSF, 1 mM DTT, and 10 mM Hepes, pH 7.4. Following dialysis, samples were snap frozen in liquid nitrogen and stored at  $-80^{\circ}\text{C}$  until use.

**Preparation of Suspended Lipid Bilayers.** All lipids as solutions in chloroform were ordered from Avanti Polar Lipids (Avanti Polar Lipids). The 1,2-diphytanoyl-*sn*-glycero-3-phosphocholine (DPhPC) and DOPE were mixed in a molar ratio of 5:3 (% mol) and chloroform was evaporated under a constant stream of N<sub>2</sub> and dried at least for 1 h under vacuum. Dry lipids were resuspended at a concentration of 25 mg/mL in *n*-decane (Sigma-Aldrich) and were used immediately or stored at  $4^{\circ}\text{C}$ . For painting of the suspended lipid bilayer, the tip of a plastic pipette (gel-loading pipette 0.1–100  $\mu$ L) was dipped into the lipid solution and successive lipid solution was ejected. Bilayers were prepared with an air bubble on the tip of the pipette formed close to the SU-8 microwell and careful painting across the opening separating *cis* and *trans* chambers. The preparation of the lipid bilayer (23) adds a  $C_{\text{MEM}}$  of ~2.5 pF, increasing  $I_{\text{rms}}$  at 500-kHz bandwidth from 10.2 to ~20.4 pA<sub>RMS</sub> (Fig. S2 A and B). Typically, the suspended lipid bilayers are stable over extended periods of time, exceeding the typical duration of an experiment (~15–30 min), and do not show any sign of leakage at potentials up to  $\pm 200$  mV. Short square-wave pulses (~1 s) at a voltage amplitude higher than 500 mV are sufficient to break the lipid bilayer, which is in good agreement with the reported values for the breakdown potential of lipid bilayer prepared using comparable lipids (40).

**Incorporation of RyR1 into Suspended Lipid Bilayers.** Fusion of proteoliposomes containing RyR1 was promoted via an osmotic gradient due to the presence of 20% (vol/vol) glycerol captured in the liposomes. The proteoliposomes were preformed as described above and subsequently mixed 1:1 (vol/vol) in 20 mM Hepes, pH 7.3, 150 mM KCl, and 40% glycerol. Samples were then subjected to repeated freeze–thaw cycles and ultrasound treatment to allow encapsulation of the glycerol in the vesicle lumen. For incorporation of the RyR1 channel into the readily prepared suspended lipid

bilayers, 1–2  $\mu$ L of the proteoliposome solution was added to the buffer in the *cis* chamber (volume ~1 mL).

**Single-Channel Recordings and Data Analysis.** Single-channel recordings at different Ca<sup>2+</sup> concentrations were performed in the presence of 20 mM Hepes, pH 7.3, 1 M KCl, 1 mM EGTA, and 1 mM (<20 nM and 40  $\mu$ M free Ca<sup>2+</sup>) or (400  $\mu$ M free Ca<sup>2+</sup>) and 5 mM ATP. Experiments were done at constant temperature of  $24^{\circ}\text{C}$ . The concentration of free Ca<sup>2+</sup> was calculated using the online resource MaxChelator and controlled using the Ca<sup>2+</sup> indicator Fura-2 pentasodium salt (Molecular Probes) and the Ca<sup>2+</sup> calibration buffer kit (Molecular Probes). The lower detection limit of the calibration curve is 15.6 nM. Using this approach, no free Ca<sup>2+</sup> was detected in the sample referred to as <20 nM. RyR1 recordings were done under a constant voltage bias of  $-200$  mV. Data were digitized at a sampling-rate of 40 million samples per second (MSps). Digital filtering of the data were performed using a software based four-pole Bessel filter at the respective filter frequencies and subsequently decimated to a sample rate of 8 times the filter frequency for each respective bandwidth. The analysis of event amplitudes and durations (Fig. 3) was done by first idealizing the data using the SKM method in QuB (21). The idealized data were then used to identify the open state events and for determining the boundaries for averaging the raw data points within the open state level, giving  $I_{\text{channel}}$ . Advanced analyses (Fig. 4) of the down-sampled (at 4 MSps) and filtered single channel recordings were performed by using QuB. Data were idealized using SKM method and rate constants were optimized using the MIL approach. A dead time of two samples (0.5  $\mu$ s) was used to correct for missed events. MIL was repeatedly run until the log likelihood (LL) did not change by more than 10 LL units. Values are the means of three runs and SD.

**ACKNOWLEDGMENTS.** The authors thank G. Thiel for critical reading and discussion of the manuscript. This work was supported in part by the W. M. Keck Foundation and by the National Institutes of Health under Grants R01HG009189 and R01HG006879 to K.L.S., P41GM116799 to W.A.H., and R01AR060037 and R01HL061503 to A.R.M. P.O. acknowledges support from the National Science Foundation Graduate Research Fellowship program under DGE 16-44869. I.S. was supported by the Deutsche Forschungsgemeinschaft under Grant SCHR 1467/1-1 and the Landes-Offensive zur Entwicklung Wissenschaftlich-oekonomischer Exzellenz (LOEWE) initiative (INAP0). M.H.G. received support from the National Heart, Lung, and Blood Institute/NIH (T32HL120826). This work was performed in part at the Advanced Science Research Center NanoFabrication Facility of the Graduate Center at the City University of New York. This work was carried out in part in the Clean Room lab of the Columbia Nano Initiative (CNI) Shared Lab Facilities at Columbia University.

- Laskowski M, et al. (2016) What do we not know about mitochondrial potassium channels? *Biochim Biophys Acta* 1857:1247–1257.
- Chacar S, Farès N, Bois P, Faivre J-F (2017) Basic signaling in cardiac fibroblasts. *J Cell Physiol* 232:725–730.
- Mittal R, et al. (2017) Indispensable role of ion channels and transporters in the auditory system. *J Cell Physiol* 232:743–758.
- Neher E, Sakmann B (1976) Single-channel currents recorded from membrane of denervated frog muscle fibres. *Nature* 260:799–802.
- Qin F (2007) Principles of single-channel kinetic analysis. *Methods Mol Biol* 403: 253–286.
- Mortensen M, Smart TG (2007) Single-channel recording of ligand-gated ion channels. *Nat Protoc* 2:2826–2841.
- Hite RK, Tao X, MacKinnon R (2017) Structural basis for gating the high-conductance Ca<sup>2+</sup>-activated K<sup>+</sup> channel. *Nature* 541:52–57.
- des Georges A, et al. (2016) Structural basis for gating and activation of RyR1. *Cell* 167:145–157.
- Ulmschneider MB, et al. (2013) Molecular dynamics of ion transport through the open conformation of a bacterial voltage-gated sodium channel. *Proc Natl Acad Sci USA* 110:6364–6369.
- Domene C, Grottesi A, Sansom MSP (2004) Filter flexibility and distortion in a bacterial inward rectifier K<sup>+</sup> channel: Simulation studies of KirBac1.1. *Biophys J* 87:256–267.
- Crozier PS, Henderson D, Rowley RL, Busath DD (2001) Model channel ion currents in NaCl-SPC/E solution with applied-field molecular dynamics. arXiv:physics/0110016.
- Shrivastava IH, Sansom MS (2000) Simulations of ion permeation through a potassium channel: Molecular dynamics of KcsA in a phospholipid bilayer. *Biophys J* 78:557–570.
- Henzler-Wildman KA, et al. (2007) A hierarchy of timescales in protein dynamics is linked to enzyme catalysis. *Nature* 450:913–916.
- Parzefall F, Wilhelm R, Heckmann M, Dudel J (1998) Single channel currents at six microsecond resolution elicited by acetylcholine in mouse myoballs. *J Physiol* 512: 181–188.
- Shapovalov G, Lester HA (2004) Gating transitions in bacterial ion channels measured at 3 microns resolution. *J Gen Physiol* 124:151–161.
- Rosenstein JK, Wanunu M, Merchant CA, Drndic M, Shepard KL (2012) Integrated nanopore sensing platform with sub-microsecond temporal resolution. *Nat Methods* 9:487–492.
- Bellinger AM, et al. (2008) Remodeling of ryanodine receptor complex causes “leaky” channels: A molecular mechanism for decreased exercise capacity. *Proc Natl Acad Sci USA* 105:2198–2202.
- Shekar S, et al. (2016) Measurement of DNA translocation dynamics in a solid-state nanopore at 100 ns temporal resolution. *Nano Lett* 16:4483–4489.
- Bellinger AM, et al. (2009) Hypernitrosylated ryanodine receptor calcium release channels are leaky in dystrophic muscle. *Nat Med* 15:325–330.
- Qin F, Li L (2004) Model-based fitting of single-channel dwell-time distributions. *Biophys J* 87:1657–1671.
- Nicolai C, Sachs F (2013) Solving ion channel kinetics with the QuB software. *Biophys Rev Lett* 08:191–211.
- Schroeder I (2015) How to resolve microsecond current fluctuations in single ion channels: The power of beta distributions. *Channels* 9:262–280.
- Rosenstein JK, Ramakrishnan S, Roseman J, Shepard KL (2013) Single ion channel recordings with CMOS-anchored lipid membranes. *Nano Lett* 13:2682–2686.
- Lindsay ARG, Manning SD, Williams AJ (1991) Monovalent cation conductance in the ryanodine receptor-channel of sheep cardiac muscle sarcoplasmic reticulum. *J Physiol* 439:463–480.
- Wagner LE, 2nd, Groom LA, Dirksen RT, Yule DI (2014) Characterization of ryanodine receptor type 1 single channel activity using “on-nucleus” patch clamp. *Cell Calcium* 56:96–107.
- Yan Z, et al. (2015) Structure of the rabbit ryanodine receptor RyR1 at near-atomic resolution. *Nature* 517:50–55.
- Clarke OB, Hendrickson WA (2016) Structures of the colossal RyR1 calcium release channel. *Curr Opin Struct Biol* 39:144–152.
- Bezprozvanny I, Watras J, Ehrlich BE (1991) Bell-shaped calcium-response curves of Ins(1,4,5)P<sub>3</sub>- and calcium-gated channels from endoplasmic reticulum of cerebellum. *Nature* 351:751–754.
- Qin J, et al. (2009) Ryanodine receptor luminal Ca<sup>2+</sup> regulation: Swapping calsequestrin and channel isoforms. *Biophys J* 97:1961–1970.

30. Mukherjee S, Thomas NL, Williams AJ (2012) A mechanistic description of gating of the human cardiac ryanodine receptor in a regulated minimal environment. *J Gen Physiol* 140:139–158.
31. Gomez AC, Yamaguchi N (2014) Two regions of the ryanodine receptor calcium channel are involved in Ca(2+)-dependent inactivation. *Biochemistry* 53:1373–1379.
32. Zalk R, et al. (2015) Structure of a mammalian ryanodine receptor. *Nature* 517:44–49.
33. Naraghi M (1997) T-jump study of calcium binding kinetics of calcium chelators. *Cell Calcium* 22:255–268.
34. Jackson AP, Timmerman MP, Bagshaw CR, Ashley CC (1987) The kinetics of calcium binding to fura-2 and indo-1. *FEBS Lett* 216:35–39.
35. Markowitz J, et al. (2005) Calcium-binding properties of wild-type and EF-hand mutants of S100B in the presence and absence of a peptide derived from the C-terminal negative regulatory domain of p53. *Biochemistry* 44:7305–7314.
36. Jensen MO, Jogini V, Eastwood MP, Shaw DE (2013) Atomic-level simulation of current-voltage relationships in single-file ion channels. *J Gen Physiol* 141:619–632.
37. Schroeder I, Thiel G, Hansen U-P (2013) Ca<sup>2+</sup> block and flickering both contribute to the negative slope of the IV curve in BK channels. *J Gen Physiol* 141:499–505.
38. Cruickshank CC, Minchin RF, Le Dain AC, Martinac B (1997) Estimation of the pore size of the large-conductance mechanosensitive ion channel of *Escherichia coli*. *Biophys J* 73:1925–1931.
39. Lee HB, Xu L, Meissner G (1994) Reconstitution of the skeletal muscle ryanodine receptor-Ca<sup>2+</sup> release channel protein complex into proteoliposomes. *J Biol Chem* 269:13305–13312.
40. Kramar P, Miklavcic D, Lebar AM (2007) Determination of the lipid bilayer breakdown voltage by means of linear rising signal. *Bioelectrochemistry* 70:23–27.